PAPER

Wearable inertial energy harvester with sputtered bimorph lead zirconate titanate (PZT) thin-film beams

IOP Publishing Smart Materials and Structures
Smart Mater. Struct. 27 (2018) 085026 (12pp) https://doi.org/10.1088/1361-665X/aad037

Wearable inertial energy harvester with sputtered bimorph lead zirconate titanate (PZT) thin-film beams

Tiancheng Xue[1], Hong Goo Yeo[2], Susan Trolier-McKinstry[2] and Shad Roundy[1]

[1] University of Utah, Department of Mechanical Engineering, 1495 E 100 S, Salt Lake City, UT, United States of America
[2] Pennsylvania State University, Materials Science and Engineering Department and Materials Research Institute, Millennium Science Complex, University Park, PA, United States of America

E-mail: tiancheng.xue@utah.edu

Received 5 April 2018, revised 15 June 2018
Accepted for publication 29 June 2018
Published 25 July 2018

Abstract

Energy harvesting from human motion addresses the growing need for self-powered wearable health monitoring systems which require 24/7 operation. Human motion is characterized by low and irregular frequencies, large amplitudes, and multi-axial motion, all of which limit the performance of conventional translational energy harvesters. An eccentric rotor-based rotational approach originally used in self-winding watches has been adopted to address the challenge. This paper presents a three-dimensional generalized rotational harvester model that considers both linear and rotational excitations. A hypothetical power upper bound for such architectures derived using this generalized model demonstrated the possibility for harvesting significantly more energy compared to existing devices. A wrist-worn piezoelectric rotational energy harvester was designed and fabricated attempting to narrow this gap between existing devices and the theoretical upper bound. The harvester utilizes sputtered bimorph PZT/nickel/PZT thin-film beams to accommodate the need for both flexibility and high piezoelectric figure of merit in order to realize a multi-beam wearable harvester. The prototype was characterized using a bench-top swing arm set-up to validate the system-level model, which provides many degrees of freedom for optimization.

Keywords: energy harvesting, piezoelectric, wearable, magnetic plucking, rotational

(Some figures may appear in colour only in the online journal)

1. Introduction

Energy harvesting is a promising alternative to batteries for powering long-term mobile health monitoring. The need to recharge batteries frequently undermines the user experience for many consumer electronics [1]. As the power consumption becomes a major obstacle to the emerging wearable market, various forms of energy harvesting from the body are being explored to reduce or eliminate battery changes [2]. Body motion, body heat and breathing are all candidates to provide a continuous power supply; each methodology entails trade-offs in terms of available power and wearability. Based on the calculation of the 'work' done, available power from human motion (on the order of Watts) is at least an order of magnitude higher than other sources [2]. However only a small portion of that energy can be actually exploited, as most of the mechanical work is produced and dissipated within the body itself. Walking, in particular, involves a cycle between kinetic energy and gravitational-potential energy to minimize chemical energy expenditure [3]. Nevertheless, harvesting inertial energy from human motion is interesting as the energy is readily accessible; other energy sources impose more requirements on environmental conditions [4–6]. For instance, thermal energy harvesting is improved when the thermoelectric device is in good thermal

contact to the skin and there is continuous airflow over the device to maintain the temperature gradient [7]. These conditions undermine the general wearability of the devices.

Harvesting inertial energy from human motion entails a number of challenges. On one hand, due to the low and irregular frequency of human motion (usually around 1 Hz [8]), resonant harvesters operating at much higher frequencies cannot directly benefit from peak dynamic magnification. Moreover, human motion contains a high amount of multi-axial movement with large displacement amplitude, whereas conventional translational harvesters are designed to be uni-directional allowing a small displacement amplitude.

Automatic self-winding watches are early successful exploitations in human-powered energy harvesting. The well-known Seiko Kinetic watch converts the kinetic energy of an eccentric rotor to electricity using a miniaturized electromagnetic generator [9]. Such eccentric rotor-based rotational designs are propitious solutions to overcome the limitation of conventional linear harvesters, as a rotor can take advantage of excitations in all directions with no inherent motion limit. An early analysis on the rotational energy harvesting approach was presented in [10]. The slow and large proof mass motion is problematic especially for electromagnetic energy harvesters due to the need to boost the low voltages produced by slow rotation. In addition, it can be difficult to achieve the optimal level of electromechanical damping for small devices. The Seiko Kinetic watch implements a sophisticated high-ratio gear train to boost the speed, and hence the voltage, but it comes with a cost of higher mechanical damping in the form of friction from high-speed bearings [11].

Another strategy, which is often referred to as frequency up-conversion, is to excite a higher-frequency resonance in a transducer via a slower-frequency motion from environmental excitation. This strategy essentially enables a resonant oscillator to operate in a non-resonant fashion. Typically the frequency up-conversion strategy is implemented in piezoelectric energy harvesters including impact-based operation [12–14], mechanical plucking via pins [15, 16] and magnetic coupling [17–21]. Methods involving mechanical contact for the excitation usually suffer from reliability problems. Therefore, a non-contact excitation such as magnetic coupling will be more suitable for long-term operation.

For piezoelectric transducers, contactless actuation through magnetic coupling is usually achieved by magnetically deflecting a piezoelectric cantilever beam and letting it ring down at its natural frequency. One of the first inertial wearable piezoelectric harvester prototypes was demonstrated in [20] using one bulk PZT beam with in-plane plucking, i.e., the beam deflects in the same plane as the moving magnet. An obvious solution to a higher power density is to implement multiple beams in one device. However, the design space of a wearable device generally allows only one bulk PZT beam due to its high stiffness. For example, the bulk PZT beam used in [20] is 370 μm in total thickness, and exhibits a resonance frequency of 400 Hz. A multi-beam architecture with bulk PZT materials is more feasible in direct force (or torque) driven harvesters where the excitation can overcome the accumulated rigidity of the cantilever beams; this can be done, for example, with knee joint motion [18, 22]. Polyvinylidene fluoride (PVDF) beams provide superior flexibility but suffer from a poor piezoelectric figure of merit for energy harvesting [23]. Therefore, the ideal candidate for inertial applications is a PZT thin-film that combines flexibility with strong piezoelectric response. A mechanically plucked 4-beam piezoelectric energy harvester was proposed using silicon-based PZT unimorph beams [16]. However, the eventual prototype has only one beam. In this work, a 10-beam harvester architecture is proposed implementing custom fabricated bimorph PZT/Ni/PZT thin-film beams. The total thickness of the bimorph is around 60 μm and exhibits a resonance frequency of 150 Hz.

This paper extends a previous analysis on the theoretical power upper bound for rotational energy harvesters [24]. A generalized three-dimensional eccentric rotor-based energy harvester model was derived to provide an estimate of the maximum power output from such harvester architectures regardless of the energy conversion mechanism. Artificial excitations constructed based on the characteristics of real-world human activities served as the inputs to the model. A previous study indicates that the upper bound on power generation from an eccentric rotor-based harvester during normal activities is approximately an order of magnitude greater than what has been demonstrated by commercial electromagnetic generators [11]. The proposed prototype in this study is intended to narrow this gap by replacing the highly damped gearing system with the contactless magnetic coupling to up-convert the frequency. The implementation of multiple beams and magnets allows for tuning the system dynamics and optimization of the system electromechanical coupling based on more design variables from a system-level harvester model. For simplicity and repeatability, the proposed harvester prototype is characterized on a bench-top motor-controlled swing arm to approximately mimic the upper limb in locomotion.

2. Generalized rotational harvester model

In order to provide an estimate of the maximum possible power generation from real-world multidimensional inputs, a full rotational harvester model in 3 dimensions is required. The planar rotational harvester model described in [10] only accounted for one rotational or linear excitation individually. This model was extended to 3 dimensions with 6 axial simultaneous inputs [24] as illustrated in figure 1. An electrical and a mechanical rotational damper are included in the model to represent extracted and lost energy respectively. The electrical damper represents any kind of ideal energy transducer and the mechanical damper represents a combined pathway for all kinds of energy losses (e.g. friction). As in many previous published studies [6, 25], this model makes the assumption that the power dissipated through an optimal viscous damper that represents the electromechanical transducer is the maximum electrical power that can be extracted from the system. The motion of the rotor is constrained in the local 2D wrist frame, and is given by:

$$m\ddot{\boldsymbol{x}} = \boldsymbol{F}_h + m\boldsymbol{g}, \tag{1}$$

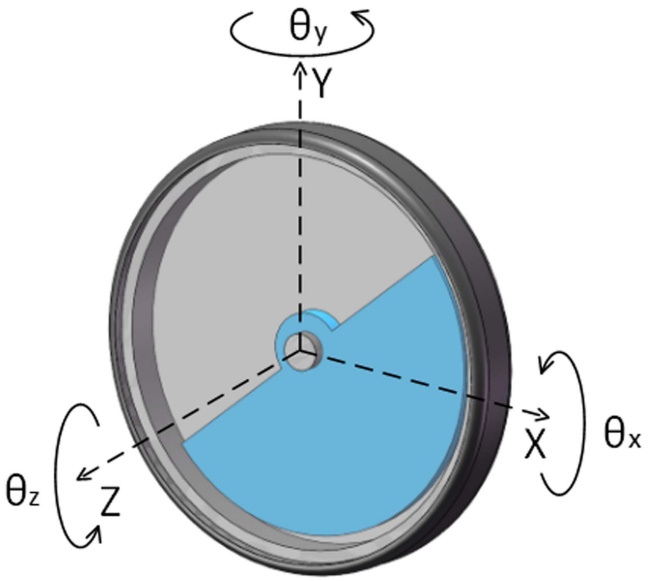

Figure 1. Schematic of the eccentric rotor based generalized rotational energy harvester model.

$$I_g\ddot{\psi}_z = T_d + (-\boldsymbol{L}) \times \boldsymbol{F}_h, \tag{2}$$

where m, I_g and $\boldsymbol{L}$ are the mass, the moment of inertia about the center of mass and the eccentricity vector of the rotor respectively. $\boldsymbol{x}$ and ψ_z are absolute linear and angular displacement of the rotor. $\boldsymbol{F}_h$ is the force acted on the rotor from the housing via the shaft and T_d is the sum of all the damping torques with respect to the center of the rotor mass. The governing equations of the generalized rotational energy harvester (see the appendix for the detailed Newtonian derivation) can be determined from equations (1) and (2) as:

$$m\begin{bmatrix} \ddot{X} - L\ddot{\psi}_z \sin\phi_z - L\dot{\psi}_z^2 \cos\phi_z \\ \ddot{Y} + L\ddot{\psi}_z \cos\phi_z - L\dot{\psi}_z^2 \sin\phi_z \end{bmatrix} = \begin{bmatrix} F_x \\ F_y \end{bmatrix} + m\begin{bmatrix} g_x \\ g_y \end{bmatrix}, \tag{3}$$

$$I_g(\ddot{\phi}_z + \ddot{\theta}_z) = -(b_m + b_e)\dot{\phi}_z + F_x L \sin\phi_z - F_y L \cos\phi_z. \tag{4}$$

Note that equation (3) was given with erroneous angular velocity and angular acceleration terms in [24] and has been corrected here. $\ddot{X}$, $\ddot{Y}$ and θ_z are linear accelerations (without gravitational components) and rotational excitation to the housing-rotor system, respectively. F_x, F_y and g_x, g_y are the forces from the housing and the gravitational accelerations acting on the rotor, respectively in each local coordinate. b_e and b_m are electrical and mechanical damping coefficients, respectively. ϕ_z denotes the relative angular displacement between the rotor and the housing, which determines the instantaneous power output as:

$$P = b_e\dot{\phi}_z^2. \tag{5}$$

Furthermore, the governing equation can be reduced to the following by analytically evaluating equations (3) and (4),

$$\ddot{\phi}_z = \frac{-(b_m + b_e)\dot{\phi}_z + mL[(\ddot{X} - g_x)\sin\phi_z - (\ddot{Y} - g_y)\cos\phi_z]}{I_g + mL^2} - \ddot{\theta}_z. \tag{6}$$

The generalized rotational harvester model provides an estimate of the maximum power output in an ideal scenario in which the electromechanical coupling can be closely approximated by an optimal linear viscous damper and mechanical damping losses and parasitic electrical losses are neglected. This may seem counterintuitive as assuming $b_m = 0$ in a linear vibration energy harvester would result in an optimal b_e of almost zero with nearly infinite displacement and power output. In this rotational case, however, there is no resonant effect as there is no restoring spring. As a result, the optimal b_e is much higher than the implemented realistic b_m as observed in simulation. Real-world constraints such as the existence of mechanical friction and the need for power conditioning will certainly lower the obtainable power.

A pseudo walking motion in the form of a trajectory generated by a one-degree-of-freedom swing arm (i.e. motor controlled pendulum) with length l_a was used as the input to the system. For a sinusoidal swing arm trajectory with an amplitude of α and a period of τ, the corresponding accelerative excitations are given by

$$\ddot{X} = -l_a\left(\frac{2\pi\alpha}{\tau}\right)^2 \cos^2\left(\frac{2\pi t}{\tau}\right), \tag{7}$$

$$\ddot{Y} = -l_a\alpha\left(\frac{2\pi}{\tau}\right)^2 \sin\left(\frac{2\pi t}{\tau}\right), \tag{8}$$

$$g_x = g\cos\left(\alpha\sin\frac{2\pi t}{\tau}\right), \tag{9}$$

$$g_y = -g\sin\left(\alpha\sin\frac{2\pi t}{\tau}\right), \tag{10}$$

where the X axis is pointing down perpendicular to the ground. As shown in figure 2, the power output was found to be a function of the electrical damping coefficient and the eccentric rotor inertia. The optimal electrical damping is dependent on both the input excitation and the rotor inertia itself. In the simulation, b_m is set to be zero as described earlier. For figure 2(a), the amplitude and the period of the input is 12.5° and 0.8 s, respectively. The amplitude of linear excitations in both directions follows the inverse-square law with respect to the period. In addition, a smaller period leads to a larger number of pendulum swings per unit time. Thus, the power is greatly reduced when the period is increased to 1.1 s as shown in figure 2(b). For simplicity, the eccentric semicircular rotor is assumed to be made of brass with a 2 mm uniform thickness; thus, the eccentricity and the inertia are reciprocally determined. For a rotor with a 1.6 cm radius, the corresponding inertia about the center of mass is 796.2 g mm^2. Note that in reality a non-uniform thickness or a non-semicircular shape can be applied to obtain an arbitrary eccentricity for a given inertia. A material with higher density such as tungsten can also be used for a larger inertia to increase the obtainable maximum power. The excitation

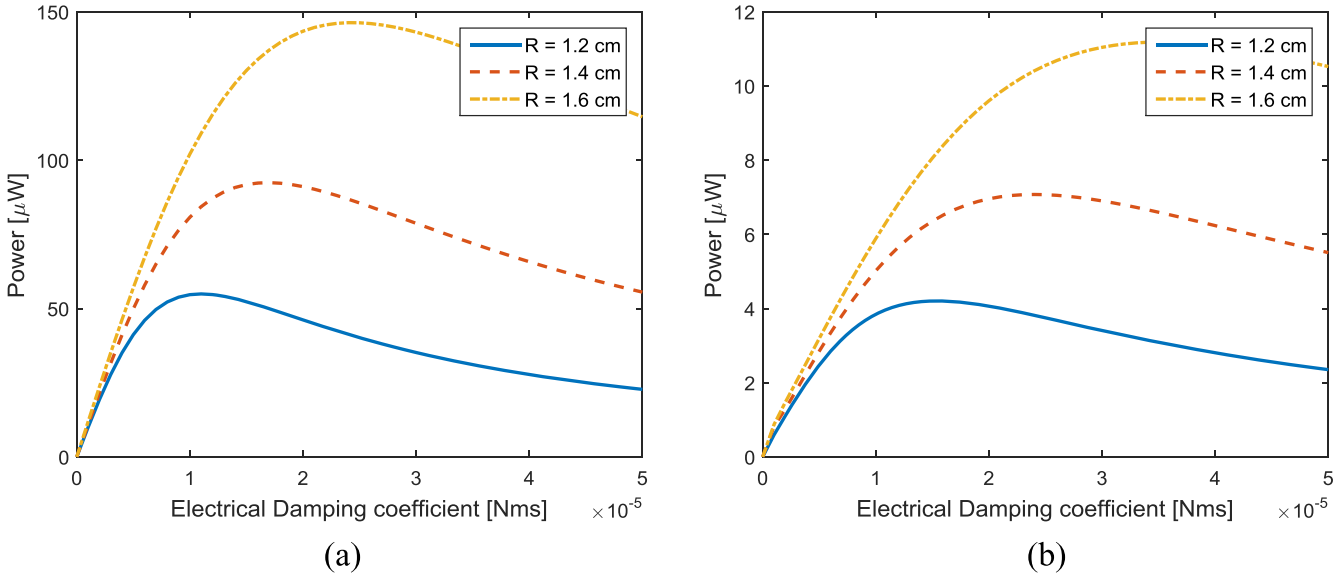

Figure 2. Calculated RMS power output as a function of electrical damping coefficient for different rotor inertia from a sinusoidal swing arm motion input: (a) amplitude = 12.5°, period = 0.8 s, (b) amplitude = 12.5°, period = 1.1 s.

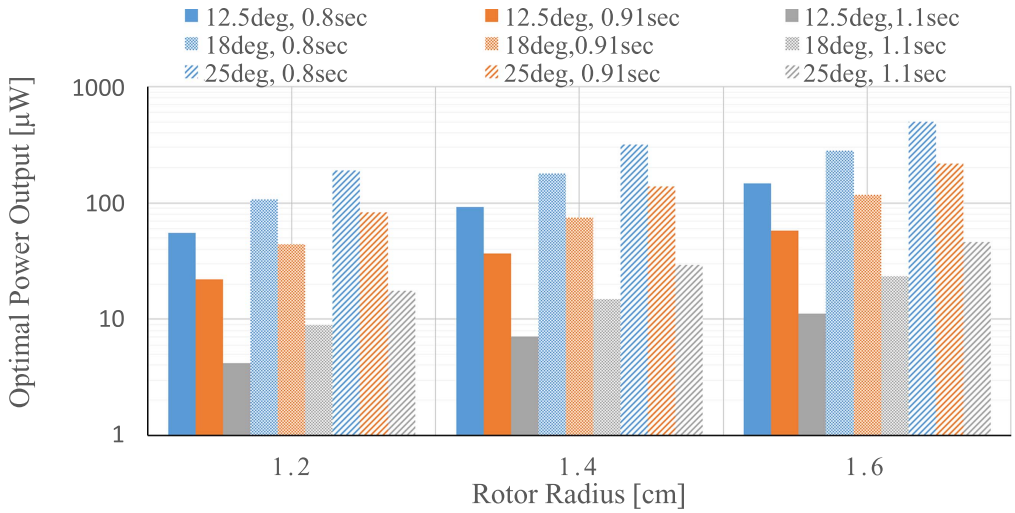

Figure 3. Upper bound on power generation for the generalized rotational harvester model from a sinusoidal swing arm motion input with different amplitudes and periods.

dependent optimal electrical damping suggests that an adaptive variable electrical damper would be preferred for real-world applications. Figure 3 illustrates the theoretical maximum power output obtained at the optimal electrical damping coefficient from a series of swing arm motions with different amplitudes and periods that correspond to various walking profiles.

3. Multi-beam harvester development

Magnetically actuated cantilever beams can be plucked in the plane or orthogonally out of the plane of the moving magnet. A comparison among different magnet configurations to achieve magnetic plucking [26] suggests that the primary advantage of out-of-plane plucking configurations in implementing a multi-beam harvester lies in the manufacturability and associated difficulty in assembly especially when the device is miniaturized. For instance, a prototype utilizing a star-shape piezoelectric element with out-of-plane plucking in [21] demonstrated the feasibility of fabricating multiple bimorph PZT beams on a single substrate. Out-of-plane plucking configurations usually lead to light electro-mechanical coupling with high dependency on the speed of moving magnet. In-plane plucking configurations provide higher coupling due to their intrinsic bifurcation in the forcing profile, especially when the velocity of the moving magnet is low [26]. The bifurcation guarantees a dynamic ring down of the piezoelectric beam to efficiently extract energy from the system. However, when the inertial excitation is weak, a strong magnetic detent torque acting on the rotor tends to inhibit the device function. In this scenario, the moving magnet fails to drive the beam beyond the bifurcation point, and hence the rotor is caught between two beams.

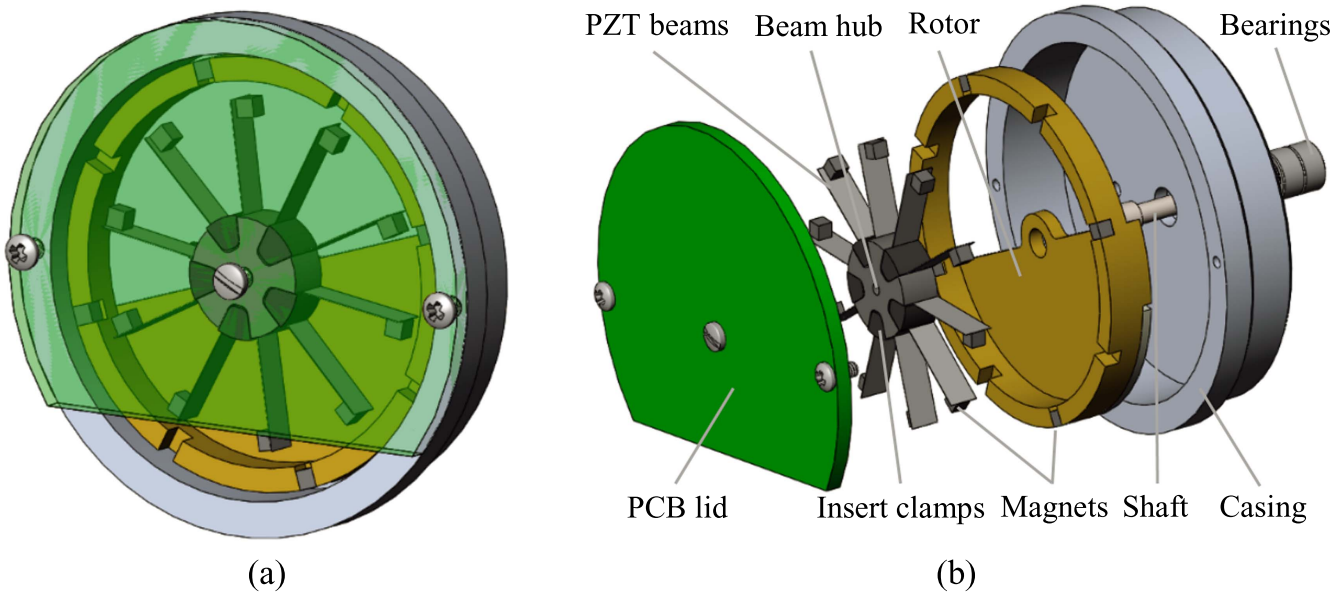

Figure 4. Rendering of the rotational energy harvester (a) in assembly and (b) in an exploded view.

Nevertheless, at lower actuation frequencies, as in the case of wrist motion, the in-plane plucking configurations outperform out-of-plane configurations assuming the inertial driving torque surpasses the detent torque.

3.1. Design and prototyping

The design of the rotational energy harvester utilizing magnetically plucked PZT thin-film beams is illustrated in figure 4. The eccentric rotor was fabricated out of brass with an outer diameter of 36 mm. Tungsten weights were glued on the outer rim of the rotor to increase mass and eccentricity. The whole proof mass weighs 13 g with a 4.63 mm eccentricity and a 2663 g mm^2 moment of inertia at the center of mass. The rotor is supported by two ball bearings (SMR52ZZ) made by Dynaroll Corporation with dimensions of 2 mm × 5 mm × 2.5 mm. The corresponding diameter of the stainless-steel shaft is 2 mm. Four neodymium N50 cube magnets with sides of length 1 mm were evenly placed and glued into the slots in the outer rim of the rotor. Note that the slots are designed to be open channels with 8 in total to allow changes in magnet arrangement in terms of size, numbers and gap to tune the system in the future. A deliberate mismatch is arranged between magnets on the rotor and magnets on the beams to avoid synchronized plucking. The synchronization at the instance of initial beam deflection is likely to induce a large detent torque on the rotor, which as mentioned earlier, restrains the rotor motion. This, however, means that each beam will require its own rectifier, which could reduce the overall efficiency of the power conditioning circuitry. 10 bimorph PZT thin-film beams were mounted in the beam hub and fastened with insert clamps. The aluminum beam hub and insert clamps were anodized to provide electrical insulation. The printed circuit board (PCB) serves not only as the lid of the prototype, but also as a robust gateway to data acquisition.

Each cantilever beam is designed with a total length of 12 mm, out of which 2 mm is clamped within the hub. An N42 cube magnet with length 1.59 mm serves as the tip mass, which reduces the active length of the beam to approximately 9.21 mm. The magnets on the beam and the rotor are designed to be in a repulsive configuration with an air gap of 1.3 mm between magnets. The piezoelectric beams were fabricated by depositing {001} oriented PZT films on both sides of a 50 μm thick flexible nickel foil. The 5 μm thick continuous bimorph PZT films were grown by high temperature *in situ rf*-magnetron sputtering with a $LaNiO_3$ (LNO) seed layer and a HfO_2 buffer layer described in [27, 28]. The final prepared film with patterned platinum electrodes is shown in figure 5(a). Individual bimorph beams were cut and hot-poled in opposite directions for a series connection. The photo of a beam sample is given in figure 5(b).

The electrical connection is made through copper tapes placed on both the beam hub and the insert clamps. Silver epoxy was added onto the beam electrodes and cured for a robust connection. Wires were soldered to the copper tapes for connection to the PCB. The copper tape has a non-conductive adhesive and is reinforced with cyanoacrylate due to its exposure to high temperature during soldering. Photos of the prototype assembly are given in figure 6. The jumper switch on the PCB can reroute one beam's output to light up a light-emitting diode from the ribbon cable connectors. Although the beams were both mechanically and electrically intact before assembly, the increase of measured capacitance of a few beams afterwards indicates a short between sandwiched layers in the beam, possibly due to excessive silver epoxy. For an individual beam, if only one electrode is shorted to the nickel shim, the beam electrically becomes a *de facto* unimorph; if both are shorted, then no power will be generated. Nevertheless, the change in electrical domain from an individual beam is unlikely to alter the overall mechanical

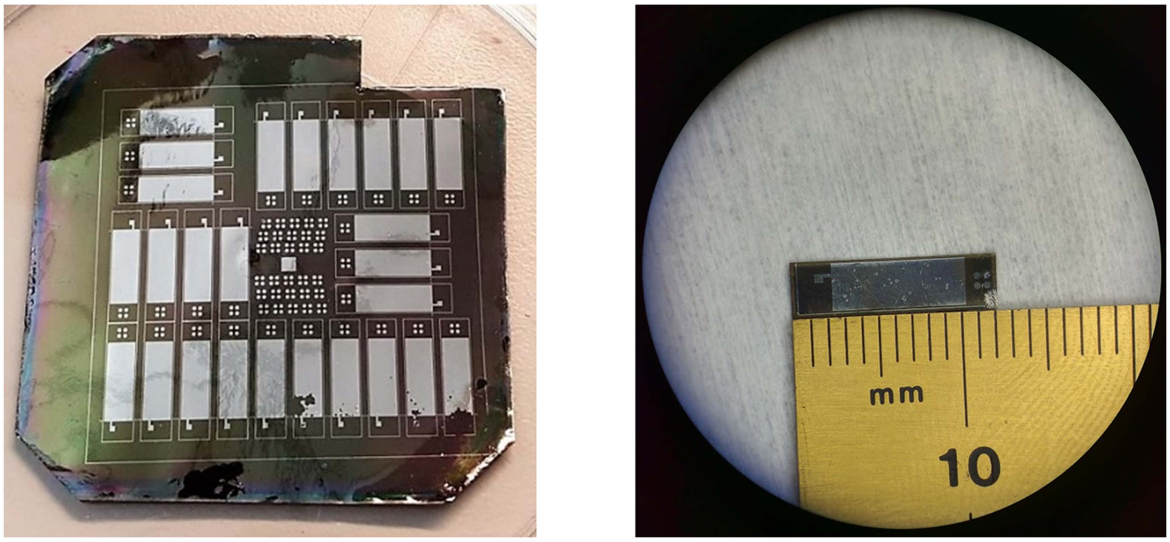

(a) (b)

Figure 5. Photo of (a) the PZT/Ni/PZT film with platinum electrodes and (b) one bimorph PZT/Ni/PZT thin-film beam.

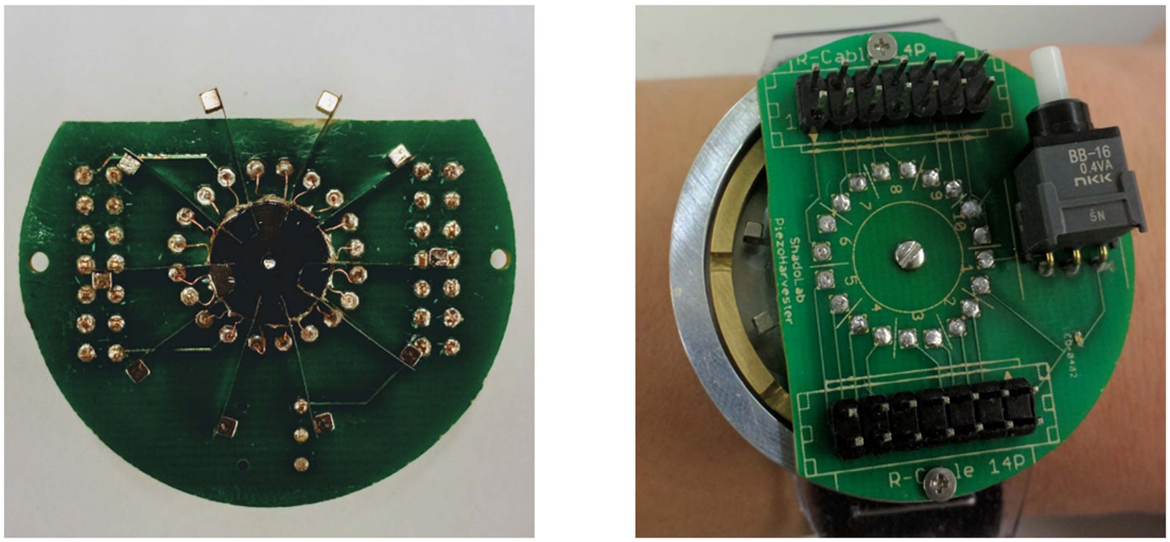

(a) (b)

Figure 6. Photo of (a) the assembled beams in the hub and (b) the assembled prototype worn on the wrist.

dynamics of the system, and thus the power output from other functional beams can be treated as unaffected.

3.2. Modeling

In order to model the system, the generalized rotational harvester model needs to be augmented with a magnetically plucked piezoelectric beam model. Many researchers have developed different approaches to formulate mathematical models for piezoelectric cantilever beams. The beam model adopted in this work has been derived in our previous work [26]. It is based on the distributed parameter model presented in [29] with a different forcing function in the form of magnetic force on the tip instead of a base excitation. Similar modeling procedures can also be found in [30]. An analytical Coulombian model was applied to calculate the force between cube permanent magnets [31] for improved accuracy as the distance between magnets is on the same order of magnitude as the dimension of magnets themselves.

The governing equation of the piezoelectric beam is given by

$$YI\frac{\partial^4 w(x,t)}{\partial x^4} + c_s I\frac{\partial^5 w(x,t)}{\partial x^4 \partial t} + c_a\frac{\partial w(x,t)}{\partial t} + m\frac{\partial^2 w(x,t)}{\partial t^2} + \left[M_t\frac{\partial^2 w(x,t)}{\partial t^2} + I_t\frac{\partial^3 w(x,t)}{\partial x \partial t^2}\right] \times \delta(x-l) - \vartheta_s v(t)\left[\frac{d\delta(x)}{dx} - \frac{d\delta(x-l)}{dx}\right] = F_m(t)\delta(x-l). \quad (11)$$

In the equation above, $w(x, t)$ is the transverse displacement of the beam. M_t and I_t are the mass and the mass moment of inertia of the proof mass, respectively. YI and l are the effective bending stiffness and the active length of the beam, respectively. c_s and c_a are the strain rate and viscous air damping coefficients, respectively. ϑ_s is the backward coupling term for a bimorph beam connected in series. $F_m(t)$ is the transverse force acting on the proof mass as a result of the magnetic coupling. $\delta(t)$ denotes the Dirac delta function. The coupled electrical circuit equation for a bimorph in the series connection is given by

$$\frac{C_p}{2}\frac{dv(t)}{dt} + \frac{v(t)}{R_l} + i_p(t) = 0, \tag{12}$$

where C_p and i_p are the internal capacitance and the corresponding current source term for one piezoelectric layer. $v(t)$ is the output voltage from the bimorph beam in the presence of a load resistance R_l.

With the introduction of the magnetically plucked piezoelectric beams in the model, the electrical damping term in the governing equation for the rotor can be replaced with the corresponding magnetic coupling as well,

$$\ddot{\phi}_z = \frac{-b_m\dot{\phi}_z + mL[(\ddot{X} - g_x)\sin\phi_z - (\ddot{Y} - g_y)\cos\phi_z] + T_m}{I_g + mL^2} - \ddot{\theta}_z, \tag{13}$$

where T_m is the sum of the magnetic torques.

In addition, relationships between the rotor displacement and the distance between each magnet pair are established with basic trigonometric approximation. The magnetic coupling is calculated based on the distance between magnets which results in a Gaussian-like function with respect to the rotor path as the rotor magnet passes one beam [26]. The entire system consists of 32 state variables from 10 piezoelectric beams and one eccentric rotor. It can be solved numerically in the time domain with proper inputs such as the sinusoidal swing arm motion mentioned earlier. Due to the intricate rotor-beam interaction, the system exhibits a strong dependence on initial conditions with high nonlinearity. Consequently, it is unlikely to obtain an exact match between simulation and measurement in the time domain. Nevertheless, the model should be able to predict the average power output over a long period of time after eliminating the effect of initial conditions.

4. Experiment

4.1. Experimental setup

As stated earlier, the chosen input for this study is a pseudo walking motion in the form of a sinusoidal one-degree-of-freedom swing arm trajectory. This artificial input carries some of the upper limb characteristics from real-world locomotion with the capability to provide rotational and accelerative excitations simultaneously. In addition, its simplicity and repeatability allow the prototype to be easily characterized against the model for corroboration.

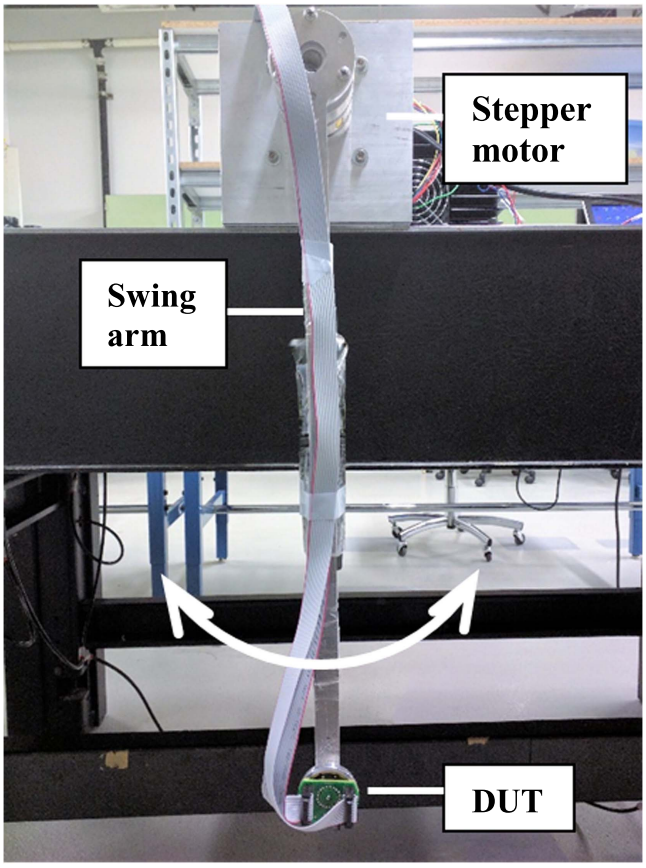

Figure 7. Photo of the swing arm test set-up with the prototype attached at the end. DUT denotes the device under test.

A bench-top motor-controlled swing arm was built to replicate a pseudo walking motion. As shown in figure 7, the 50 cm long aluminum arm roughly mimics the human upper limb. The microstepping-enabled stepper motor creates varying motion profiles in a sinusoidal fashion with different amplitudes and periods as an approximation of various walking profiles. The prototype was characterized with all the motion profiles applied earlier in the simulation of the generalized rotational harvester model. Each beam is terminated with a load resistor and the data acquisition is carried out with a PC oscilloscope.

4.2. Experimental results

A separate beam validation test was conducted beforehand in which the beam was manually deflected at the tip and released to undergo a damped oscillation. The tip displacement (via a laser displacement sensor) and the open circuit voltage output were measured simultaneously. Whereas the permittivity was calculated from the measured capacitance, the piezoelectric coefficient d_{31} can be obtained by matching the simulation to the measurement. For the particular beam shown in figure 8, the d_{31} is characterized as $-28\,\mathrm{pC\,N^{-1}}$. Overall the d_{31} of the beams distribute in a range from -25 to $-35\,\mathrm{pC\,N^{-1}}$. The low values for the effective piezoelectric coefficients are

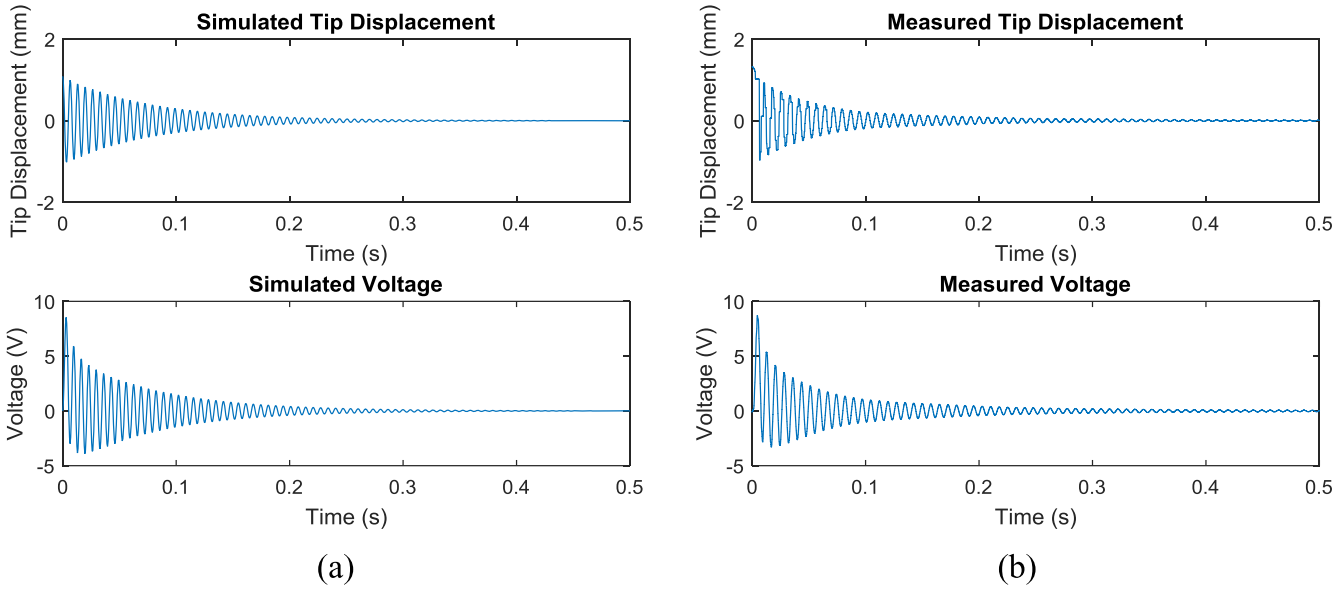

Figure 8. Individual beam validation of damped oscillation: (a) simulation versus (b) measurement.

believed to be a result of defects induced during the poling and device assembly, along with variations in the initial beam curvature due to handling. In addition, the damping ratio of the cantilever beam can be determined via the logarithmic decrement method. These parameters will be fed back to the system level model. A detailed list of parameters for the piezoelectric beam used in simulation is given in table 1.

Figure 9(a) gives an example of measured voltage output from one beam with a 150 kΩ resistive load under the sinusoidal swing arm excitation with a 25° amplitude and a 0.8 s period. A close-up view with two beam plucks is given in figure 9(b). A shift in polarity of the initial peak voltage indicates the change in plucking direction. By examining the measured waveforms, all the beams exhibit a resonant frequency between 130 and 155 Hz whereas the model indicates 150 Hz, which is reasonably good agreement given the variation in beam properties (e.g. resting curvature and electrode/hole distribution) and mounting conditions.

The prototype demonstrates a significant beam to beam variation in terms of power output although the piezoelectric coefficients are close among all the beams. This variation is likely due to inaccuracies in assembly, especially the gap between magnets, which governs the maximum strain in the beam and its voltage output via the piezomagnetoelastic coupling. The potential differences in degradation among the beams during assembly and testing could also contribute to the variation as well. Therefore, parameters are evaluated as an average value among all beams for simulation to be compared with measured result on a system level. The optimal load resistance has been identified as 150 kΩ for most beams, which corroborates the impedance match based on the measured capacitance of 7 nF per bimorph on average.

The total power output from a series of sinusoidal swing arm excitations is given in figure 10. The simulated power output is multiplied by a factor of 0.9 in order to achieve a fair comparison with simulation as one beam out of 10 is shorted

Table 1. Parameters for the bimorph PZT/Ni/PZT beam.

Parameter	Symbol	Value
Active length	l	9.2 mm
Width	b	3.0 mm
Thickness of Ni layer	h_s	50 μm
Thickness of PZT layer	h_p	5 μm
Density of Ni	ρ_s	8900 kg m^{-3}
Density of PZT	ρ_p	7500 kg m^{-3}
Young's modulus of Ni	Y_s	200×10^9 N m^{-2}
Young's modulus of PZT	$\bar{c}_{11}^E$	70×10^9 N m^{-2}
Piezoelectric coefficient	d_{31}	-30×10^{-12} m V^{-1}
Capacitance of PZT layer	C_p	12 nF
Load resistance	R_l	150 kΩ

in the prototype. Note that the excitation of 18° and 0.91 s generates no power. As a matter of fact, the harvester does not function in either simulation or experiment under any weaker excitation, including the excitation of 12.5° and 0.91 s, and all 3 excitations with a period of 1.1 s. In those scenarios the excitation is not strong enough to overcome the magnetic detent torque and to push the rotor through the bifurcation point of the first beam to be plucked. Consequently, the rotor is trapped between two beams and does not produce any power. For stronger excitations, the power output generally scales with the intensity of the excitation. A total power output of approximately 40 μW can be generated from the excitation of 25° and 0.8 s, which can be seen as a pseudo fast walking profile.

Note that the d_{31} of -30 pC N^{-1} does not represent the optimal performance of such PZT material. Previous fabrications indicate a d_{31} of up to -110 pC N^{-1} can be achieved from the sputtered high-density PZT thin-films [21] (for reference, commercial bulk PZT exhibits higher d_{31}, e.g., -190 pC N^{-1} from PSI-5A4E by Piezo Systems [32]). Thus,

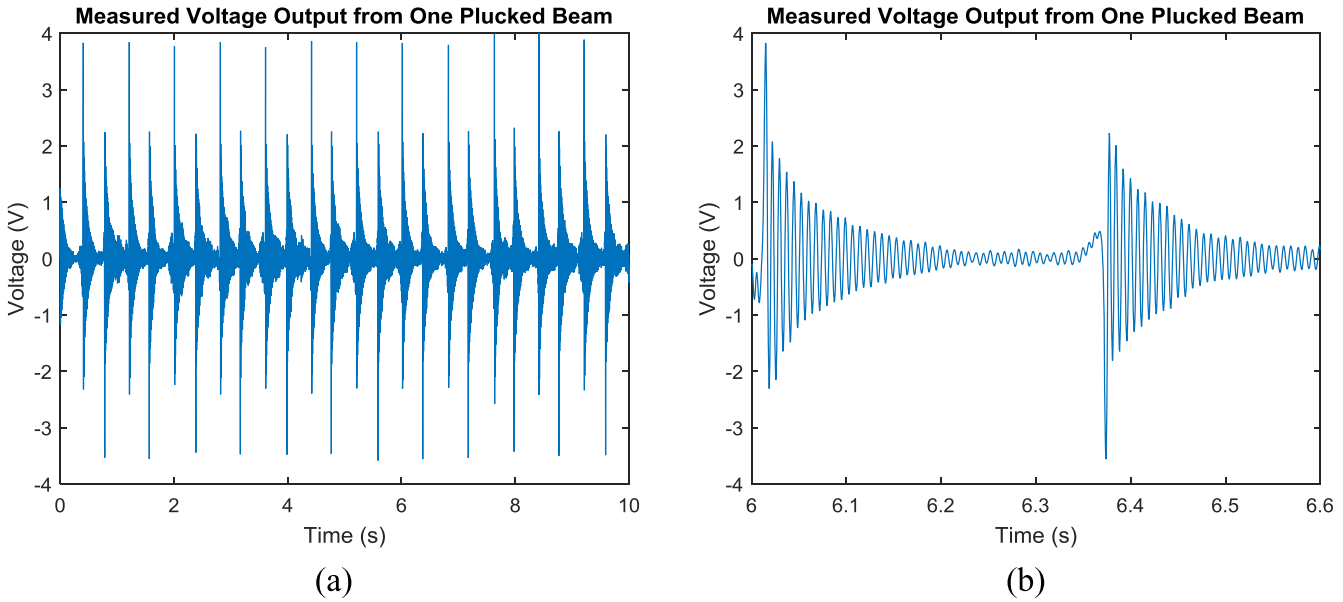

Figure 9. Measured voltage output from one beam during operation: (a) in 10 s and (b) in a close-up view.

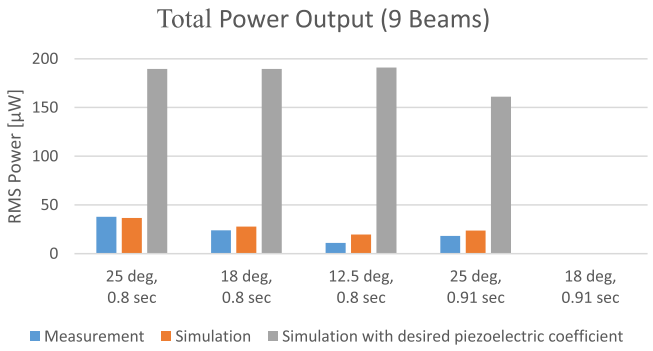

Figure 10. Average RMS power output per beam under different excitations from measurement and simulation.

a simulation with a higher piezoelectric coefficient of $-110\,\mathrm{pC\,N^{-1}}$ was conducted as well to investigate the potential of such architecture with improved material properties. In the simulation with the higher d_{31}, the 3 excitations with a period 0.8 s generate a total power output of roughly 230 μW consistently (assume 10 functioning beams) whereas the excitation of 25° and 0.91 s generates slightly less power output. This is different from the power scaling with the lower d_{31} value where the power output decreases as the excitation is reduced. The discrepancy in power scaling between different piezoelectric coefficients can be interpreted with a potential-well analogy, which is conceptually illustrated in figure 11. Figure 11(a) corresponds to the blue and orange bars with lower d_{31} ($-30\,\mathrm{pC\,N^{-1}}$) whereas figure 11(b) corresponds to the gray bar with higher d_{31} ($-110\,\mathrm{pC\,N^{-1}}$). The apparent damping torque experienced by the rotor is plotted against the excitation torque produced by the sinusoidal swing arm motion on the linear map of rotor displacement in a quasi-static fashion. On one hand, the total apparent damping consists of both the frictional mechanical damping from the bearings and the electrical damping imposed by the electromechanical coupling from the PZT bimorph, the latter of which is location dependent due to the discrete existence of piezoelectric beams. On the other hand, the excitation torque is the largest when the arm is pointing down to the ground and decreases as the arm moves up sidewise. As observed in both simulation and experiment, after the initial transient period with a cold start, the rotor will eventually go into a periodic oscillation that tracks the sinusoidal swing arm excitation in steady state. Thus, the excitation torque can be qualitatively plotted as a concave function of the rotor displacement as well. Figure 11 visually illustrates the failure points (the boundary between solid lines and dotted lines) where the excitation torque fails to overcome the apparent damping torque, which correspond to the steady-state rotor displacement limit in the dynamic simulation.

A potential well is established by two local maximum damping points described by the system which constrains the rotor motion. Each beam imposes a local maximum damping at its location where the rotor needs to overcome the magnetic detent torque. It has been shown that the energy produced per pluck for one beam is more or less consistent, with only marginal improvement with respect to the increase in the proof mass velocity [26]. This indicates that the total power output can be seen as a measurement of the number of plucks, which is determined by the rotor displacement limit per cycle per unit time. Therefore, a more distant potential well from the zero-displacement point grants a higher achievable power output for a given driving frequency. Note that the potential wells are higher in figure 11(b) than in figure 11(a) due to a higher piezoelectric coefficient d_{31}. Consequently, the same excitation is not necessarily trapped in the same potential well. For instance, the excitation of 25° and 0.8 s jumps into the third potential well in figure 11(a), whereas it is trapped in the second potential well in figure 11(b) due to an increased apparent damping. The excitation of 18° and 0.91 s falls into the potential well at zero displacement in both cases, indicating that the rotor motion is

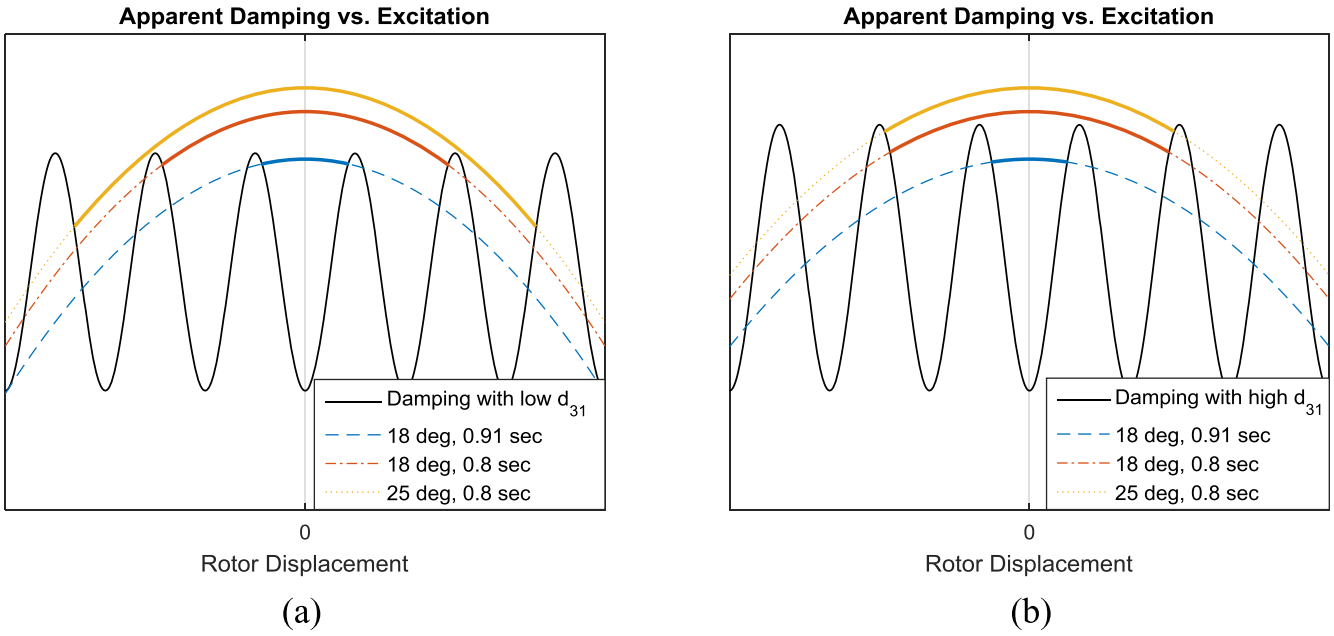

Figure 11. Characteristics of the piezoelectric harvester with a potential-well analogy.

constrained between the adjacent two beams and no power is produced. Qualitatively this agrees with the results in figure 10.

The potential-well analogy illustrates a staircase function-like system response to a sinusoidal swing arm excitation in terms of power output. There is an excitation threshold for the harvester to function governed by the mechanical damping and the electromechanical coupling. An inherent trade-off exists between the function threshold and the maximum achievable power. A smaller mechanical damping will certainly lower the threshold to function. Given the same mechanical damping, a prototype capable of functioning under weaker excitation will suffer from a lower saturation power due to its associated weaker electromechanical coupling. Nevertheless, the system can be tuned with respect to its electromechanical damping to approach optimal power output for a given input. This can be easily achieved by adjusting the magnet configuration, i.e., the gap between and the size of magnets. Furthermore, by comparing the simulated power output with $d_{31} = -110\,\mathrm{pC\,N^{-1}}$ to the theoretical power upper bound, it is clear that among excitations with a period of 0.8 s, the design with higher electromechanical coupling is more effective [33] towards the excitation of 12.5°, achieving a higher ratio of generated power to theoretical limit. The generalized rotational harvester model predicts a theoretical upper bound power output of 1419 μW and 424 μW for the excitation of 25° and 12.5° with the period of 0.8 s, respectively for the same rotor inertia. However, the actual plucked piezoelectric beam harvester can produce 230 μW for each of these excitations.

5. Conclusions

This paper presents a wearable inertial energy harvester utilizing a rotational proof mass and magnetically plucked piezoelectric beams, which specifically caters to harvesting energy efficiently from human motion. Compared to commercial electromagnetic energy harvesters such as the Seiko Kinetic watch, a frequency up-converting piezoelectric harvester not only reduces mechanical friction from the gearing system, but also provides useful voltage at low proof mass velocities. A three-dimensional generalized rotational energy harvester model is derived as the basis of the model for the proposed harvester and to predict the upper bound power output. The generalized rotational harvester model makes the assumption that the optimal transducer can be modeled as a viscous damper. It is found that for a given excitation, an optimal level of electrical damping is required to achieve the maximum power output. In general power output scales with the eccentric proof mass inertia. In real-world applications, the power upper bound will be reduced with increased mechanical damping primarily from friction.

Sputtered bimorph PZT/Ni/PZT thin-films were fabricated as the piezoelectric transducers for the harvester prototype. Compared to off-the-shelf piezoelectric products, these beams provide the appropriate combination of stiffness and material figure of merit for energy harvesting. The 10-beam prototype is characterized on a bench-top swing arm set-up with a system level model that incorporates the rotor dynamics, the electromechanical governing equation of a piezoelectric beam and the analytical magnet model. The swing arm generates a series of sinusoidal excitations that mimics the human upper limb in locomotion, which is a more representative excitation than linear base excitation with respect to wearable energy harvesters. A good match between simulation and measurement is achieved considering the inaccuracy in assembly and the beam to beam variation due to degradation. Under the sinusoidal excitation of 25° and 0.8 s, the prototype generates approximately 40 μW whereas the

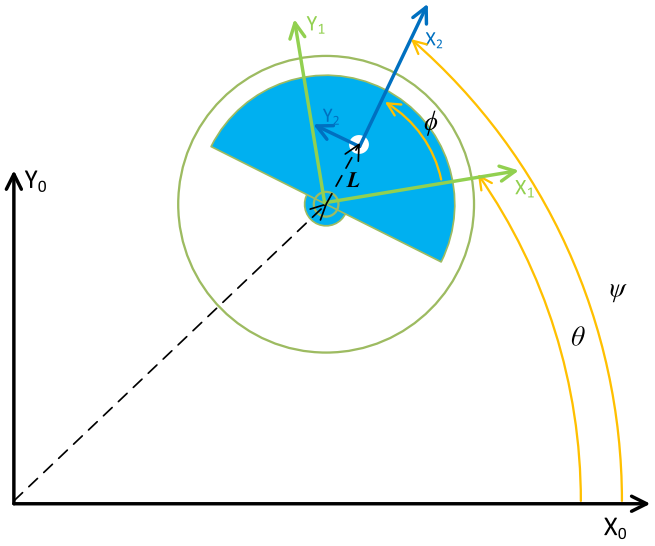

Figure A1. Schematic of the generalized rotational harvester model, θ is the rotational excitation to the system, ϕ is the relative rotation of the rotor and ψ is the absolute rotation of the rotor.

simulation suggests a 230 μW power output can be obtained with a higher but achievable piezoelectric coefficient.

Finally, the characteristics of the harvester prototype are investigated using a potential-well analogy, which provides a reasonable interpretation of measured and simulated power output under different excitations. An intrinsic trade-off between the function threshold and the maximum achievable power is identified for this architecture. The system can be further tuned to approach optimal operation for a given harmonic input. In real-world wrist-worn scenarios, however, the harvester will benefit from the ubiquitous non-periodic excitations that will help overcome the function threshold issue.

Acknowledgments

This work was supported by National Science Foundation (United States) through the NSF Nanosystems Engineering Research Center (NERC) for Advanced Self-Powered Systems of Integrated Sensors and Technologies (ASSIST) under award number EEC 1160483.

Appendix

In this discussion, the directional subscripts for rotational variables are dropped since the problem is constrained in the local X_1Y_1 wrist plane (see figure A1). The absolute acceleration of the rotor can be expressed as

$$\boldsymbol{a}_{abs} = \ddot{\boldsymbol{x}} = \boldsymbol{a}_{ref} + \ddot{\boldsymbol{\theta}} \times \boldsymbol{L} + \dot{\boldsymbol{\theta}} \times (\dot{\boldsymbol{\theta}} \times \boldsymbol{L}) + 2\dot{\boldsymbol{\theta}} \times \boldsymbol{v}_{rel} + \boldsymbol{a}_{rel}, \tag{A.1}$$

where $\boldsymbol{a}_{ref}$ and $\boldsymbol{a}_{rel}$ are the absolute acceleration of housing, measured from the global inertial frame, and the relative acceleration of the rotor with respect to the housing. $\boldsymbol{v}_{rel}$ is the relative velocity of the rotor with respect to the housing. All the vectors in equation (A.1) can be expressed with the Cartesian components along X_1, Y_1, and Z_1 axes as

$$\begin{aligned}\ddot{\boldsymbol{\theta}} \times \boldsymbol{L} &= \ddot{\theta}\boldsymbol{k}_1 \times L(\cos\phi\boldsymbol{i}_1 + \sin\phi\boldsymbol{j}_1) \\ &= L\ddot{\theta}(-\sin\phi\boldsymbol{i}_1 + \cos\phi\boldsymbol{j}_1),\end{aligned} \tag{A.2}$$

$$\begin{aligned}\dot{\boldsymbol{\theta}} \times (\dot{\boldsymbol{\theta}} \times \boldsymbol{L}) &= \dot{\theta}\boldsymbol{k}_1 \times (\dot{\theta}\boldsymbol{k}_1 \times L(\cos\phi\boldsymbol{i}_1 + \sin\phi\boldsymbol{j}_1)) \\ &= L\dot{\theta}^2(-\cos\phi\boldsymbol{i}_1 - \sin\phi\boldsymbol{j}_1),\end{aligned} \tag{A.3}$$

$$\begin{aligned}2\dot{\boldsymbol{\theta}} \times \boldsymbol{v}_{rel} &= 2\dot{\theta}\boldsymbol{k}_1 \times L\dot{\phi}(-\sin\phi\boldsymbol{i}_1 + \cos\phi\boldsymbol{j}_1) \\ &= 2L\dot{\theta}\dot{\phi}(-\cos\phi\boldsymbol{i}_1 - \sin\phi\boldsymbol{j}_1),\end{aligned} \tag{A.4}$$

$$\begin{aligned}\boldsymbol{a}_{rel} &= (-L\dot{\phi}^2\cos\phi - L\ddot{\phi}\sin\phi)\boldsymbol{i}_1 \\ &\quad + (-L\dot{\phi}^2\sin\phi + L\ddot{\phi}\cos\phi)\boldsymbol{j}_1.\end{aligned} \tag{A.5}$$

In addition, acceleration of the housing can be expressed along X_1 and Y_1 axes, which corresponds to the linear acceleration measured by the accelerometer if it is attached to the housing,

$$\boldsymbol{a}_{ref} = \ddot{X}\boldsymbol{i}_1 + \ddot{Y}\boldsymbol{j}_1. \tag{A.6}$$

Substitute equations (A.2)–(A.6) into equation (A.1),

$$\begin{aligned}\boldsymbol{a}_{abs} &= (\ddot{X} - L\ddot{\psi}\sin\phi - L\dot{\psi}^2\cos\phi)\boldsymbol{i}_1 \\ &\quad + (\ddot{Y} - L\ddot{\psi}\cos\phi - L\dot{\psi}^2\sin\phi)\boldsymbol{j}_1.\end{aligned} \tag{A.7}$$

Similarly, the gravity vector can also be expressed along X_1 and Y_1 axes as,

$$\boldsymbol{g} = g_x\boldsymbol{i}_1 + g_y\boldsymbol{j}_1. \tag{A.8}$$

The governing equation can be obtained by substituting equations (A.7) and (A.8) into (1) and (2),

$$\ddot{\psi} = \frac{-(b_m + b_e)\dot{\phi} + mL[(\ddot{X} - g_x)\sin\phi - (\ddot{Y} - g_y)\cos\phi]}{I_g + mL^2} \tag{A.9}$$

which is equivalent to equation (6).

ORCID iDs

Tiancheng Xue https://orcid.org/0000-0002-3235-7536

References

[1] Ballard B 2007 *Designing the Mobile User Experience* (New York: Wiley) (https://doi.org/10.1145/1453805.1453841)
[2] Starner T 1996 Human-powered wearable computing *IBM Syst. J.* **35** 618–29
[3] Cavagna G A, Heglund N C and Taylor C R 1977 Mechanical work in terrestrial locomotion: two basic mechanisms for minimizing energy expenditure *Am. J. Physiol.* **233** R243–61
[4] Starner T and Paradiso J A 2004 Human generated power for mobile electronics *Low-Power Electron.* **1990** 1–30
[5] Roundy S, Wright P K and Rabaey J 2003 A study of low level vibrations as a power source for wireless sensor nodes *Comput. Commun.* **26** 1131–44

[6] Mitcheson P D, Yeatman E M, Rao G K, Holmes A S and Green T C 2008 Energy harvesting from human and machine motion for wireless electronic devices *Proc. IEEE* **96** 1457–86
[7] Hyland M, Hunter H, Liu J, Veety E and Vashaee D 2016 Wearable thermoelectric generators for human body heat harvesting *Appl. Energy* **182** 518–24
[8] Yun J, Patel S N, Reynolds M S and Abowd G D 2011 Design and performance of an optimal inertial power harvester for human-powered devices *IEEE Trans. Mob. Comput.* **10** 669–83
[9] Hayakawa M 1991 Electronic wristwatch with generator *US Patent* US5001685A
[10] Yeatman E M 2008 Energy harvesting from motion using rotating and gyroscopic proof masses *Proc. Inst. Mech. Eng.* C **222** 27–36
[11] Xue T, Kakkar S, Lin Q and Roundy S 2016 Characterization of micro-generators embedded in commercial-off- the-shelf watches for wearable energy harvesting *Proc. SPIE* **9801** 98010O
[12] Renaud M, Fiorini P, van Schaijk R and van Hoof C 2009 Harvesting energy from the motion of human limbs: the design and analysis of an impact-based piezoelectric generator *Smart Mater. Struct.* **18** 035001
[13] Ju S and Ji C-H 2015 Piezoelectric vibration energy harvester using indirect impact of springless proof mass *J. Phys.: Conf. Ser.* **660** 012122
[14] Gu L and Livermore C 2011 Impact-driven, frequency up-converting coupled vibration energy harvesting device for low frequency operation *Smart Mater. Struct.* **20** 045004
[15] Pozzi M, Aung M S H, Zhu M, Jones R K and Goulermas J Y 2012 The pizzicato knee-joint energy harvester: characterization with biomechanical data and the effect of backpack load *Smart Mater. Struct.* **21** 075023
[16] Lockhart R, Janphuang P, Briand D and De Rooij N F 2014 A wearable system of micromachined piezoelectric cantilevers coupled to a rotational oscillating mass for on-body energy harvesting *Proc. IEEE Int. Conf. Micro Electro Mech. Syst.* pp 370–3
[17] Galchev T, Aktakka E E and Najafi K 2012 A piezoelectric parametric frequency increased generator for harvesting low-frequency vibrations *J. Microelectromech. Syst.* **21** 1311–20
[18] Pozzi M 2016 Magnetic plucking of piezoelectric bimorphs for a wearable energy harvester *Smart Mater. Struct.* **25** 045008
[19] Luong H T and Goo N S 2012 Use of a magnetic force exciter to vibrate a piezocomposite generating element in a small-scale windmill *Smart Mater. Struct.* **21** 025017
[20] Pillatsch P, Yeatman E M and Holmes A S 2014 A piezoelectric frequency up-converting energy harvester with rotating proof mass for human body applications *Sensors Actuators* A **206** 178–85
[21] Xue T and Roundy S 2015 Analysis of magnetic plucking configurations for frequency up-converting harvesters *J. Phys.: Conf. Ser.* **660** 012098
[22] Kuang Y, Yang Z and Zhu M 2016 Design and characterisation of a piezoelectric knee-joint energy harvester with frequency up-conversion through magnetic plucking *Smart Mater. Struct.* **25** 085029
[23] Yeager C B, Ehara Y, Oshima N, Funakubo H and Trolier-McKinstry S 2014 Dependence of $e_{31,f}$ on polar axis texture for tetragonal $Pb(Zr_x,Ti_{1-x})O_3$ thin films *J. Appl. Phys.* **116** 104907
[24] Xue T, Ma X, Rahn C and Roundy S 2014 Analysis of upper bound power output for a wrist-worn rotational energy harvester from real-world measured inputs *J. Phys.: Conf. Ser.* **557** 012090
[25] Halvorsen E, Le C P, Mitcheson P D and Yeatman E M 2013 Architecture-independent power bound for vibration energy harvesters *J. Phys.: Conf. Ser.* **476** 117–21
[26] Xue T and Roundy S 2017 On magnetic plucking configurations for frequency up-converting mechanical energy harvesters *Sensors Actuators* A **253** 101–11
[27] Yeo H G and Trolier-McKinstry S 2014 {001} Oriented piezoelectric films prepared by chemical solution deposition on Ni foils *J. Appl. Phys.* **116** 014105
[28] Yeo H G, Ma X, Rahn C and Trolier-McKinstry S 2016 Efficient piezoelectric energy harvesters utilizing (001) textured bimorph PZT films on flexible metal foils *Adv. Funct. Mater.* **26** 5940–6
[29] Erturk A and Inman D J 2009 An experimentally validated bimorph cantilever model for piezoelectric energy harvesting from base excitations *Smart Mater. Struct.* **18** 025009
[30] Pillatsch P, Yeatman E M and Holmes A S 2014 Magnetic plucking of piezoelectric beams for frequency up-converting energy harvesters *Smart Mater. Struct.* **23** 25009
[31] Akoun G and Yonnet J 1984 3D analytical calculation of the forces exerted between two cuboidal magnets *IEEE Trans. Magn.* **MAG-20** 1962–4
[32] Piezo Systems, PSI-5A4E Piezoceramic Sheets and Plates, https://perma.cc/NB92-JBZA (Accessed: 19 March 2018)
[33] Roundy S 2005 On the effectiveness of vibration-based energy harvesting *J. Intell. Mater. Syst. Struct.* **16** 809–23